Improved EBSD indexation accuracy by considering energy distribution of diffraction patterns

Qiwei Shi, Liyao Jiao, Dominique Loisnard, Chengyi Dan, Zhe Chen, Haowei Wang, Stéphane Roux

Improved EBSD indexation accuracy by considering energy distribution of diffraction patterns

Qiwei Shi[1,2], Liyao Jiao[1], Dominique Loisnard[3], Chengyi Dan[2],
Zhe Chen[2], Haowei Wang[2], Stéphane Roux[4]
1: SJTU-Paris Elite Institute of Technology,
Shanghai Jiao Tong University, Shanghai, 200240, China
2: School of Materials Science and Engineering,
Shanghai Jiao Tong University, Shanghai, 200240, China
3: EdF R&D, Site des Renardières, avenue des Renardières,
Ecuelles, F-77818 Moret-sur-Loing, France
4: Université Paris-Saclay, ENS Paris-Saclay, CNRS,
LMT - Laboratoire de Mécanique et Technologie, F-91190, Gif-sur-Yvette, France

Received: date / Accepted: date

Abstract

Registering experimental and simulated electron diffraction patterns is increasingly used for advanced electron backscatter diffraction indexation (EBSD) analysis, yet the accuracy of registration is limited by several effects not accounted for in pattern simulation, such as the Kikuchi band asymmetry, gray level reversal, optical distortion and non-uniform electron energy. Though some of these phenomena can be simulated by Monte Carlo method and dynamical simulation, the computation is highly demanding and their effects on EBSD calibration are seldom analyzed. Here a simple weighting of energy for simulated diffraction pattern is proposed based on several master patterns calculated before-hand, to effectively account for the electron energy distribution. Integrated digital image correlation is alternatively applied to quantify the electron energy field and calibrate geometry parameters. A metric of the *accuracy* of indexed crystal orientation is proposed based on a large-area high-definition experimental EBSD acquisition on a (100)-face single crystal Si wafer. The consideration of inhomogeneous energy distribution reduces the crystal orientation discrepancy by 0.128° for the Si dataset.

Keyword: EBSD calibration, High-angular-resolution EBSD, Integrated digital image correlation, electron energy distribution, error analysis.

1 Introduction

Electron BackScatter Diffraction (EBSD) technique has evolved as a technique of choice to obtain crystallographic orientation fields in scanning electron microscopes. This technique aims principally at obtaining orientation maps from the analysis of the Kikuchi diffraction pattern (thereafter denoted as EBSP for Electron BackScatter Pattern) by Hough-transformation [1] or the newly emerged convolutional neural network [2]. Standard EBSD usually provides results with an angular resolution of about 0.5°. Such an uncertainty is sufficient to evaluate local orientation maps but cannot reveal elastic strains or small angle grain boundaries, which are associated with low deformations of diffraction images.

High-(angular) Resolution EBSD (HR-EBSD) — exploiting high-definition EBSPs registered onto a reference one through Digital Image Correlation (DIC) — has been proposed to obtain *relative* crystallographic orientations with a much higher accuracy [3, 4]. It has been shown that HR-EBSD enables the elastic strains to be measured with acceptable uncertainties and excellent spatial resolution [5]. Both *local* DIC algorithm based on cross-correlation [3] and *(integrated) global* DIC framework [6, 7, 8, 9] have been adopted in HR-EBSD. The latter method proves fast and precise for both simulated and experimental EBSPs. Global DIC can also measure grain-level absolute stress without simulated reference EBSP [10]. Yet, for both algorithms, the final results of HR-EBSD are limited by the accuracy of the projection parameters [11, 8].

Full pattern matching (FPM) EBSD calibration methods have known a rapid progress in the recent years. The basic idea is to tune the projection parameters (in particular the three coordinates of the PC and the Euler angles of crystal orientation) in order to maximize the similarity between experimental and simulated EBSPs. *Dynamical* EBSP simulation proves to have a higher similarity with experimental pattern than *kinematic* simulations [12]. To achieve the optimization of the projection parameters, many algorithms have been suggested, such as a Nelder-Mead algorithm [13, 14, 15], cross-correlation with log-polar transform [16], evolution algorithm [17], SNOBFIT algorithm [15], integrated DIC algorithm [18] or non-disclosed ones used in commercial software [19]. IDIC is able to calibrate overlapped EBSPs at grain boundaries, to obtain multiple sets of Euler angles, one set of PC and the contribution ratio for each crystal orientation [20]. The PC calibration uncertainty has been shown to reach values as low as 10^{-5} times the pattern width for simulated EBSPs. The reported Euler angles uncertainty is also very low: 0.03° for a 640×480 pixel EBSP used for the analysis of a tungsten carbide sample [21]. The same crystal orientation uncertainty level is obtained at grain boundaries for both grains [20].

However, different groups studying FPM EBSD calibration on polycrystal samples have very recently reported grainwise discontinuity in PC fields [15, 18]. The shift of PC components across grain boundaries could reach 1-2 pixels, that cannot be due to the sample topography nor to the elastic strain. This intriguing phenomenon highlights the imperfection of registering experimental EBSP with a simple projection of simulated master pattern. Researchers have pointed out several secondary effects in experimental EBSPs that need to be considered. For example, the brightness of Kikuchi band is closely linked to the sample tilt angle, and when the latter is smaller than 60°, it could even lead to reversed gray level distributions [22]. Recent studies have also reported the inhomogeneous distribution of backscattered electron (BSE) energy [23, 24], explicitly, that of electrons diffracted to the top of the detector is several keV lower than that of the bottom. Horizontal Kikuchi bands have brighter upper edges and

darker lower ones, a phenomenon named excess-deficiency (abbreviated as ED hereinafter). This effect is due to the anisotropic diffracted electron distribution, a phenomenon well described in Ref. [25]. If these secondary effects are not accounted for, *systematic* errors in PC and crystal orientation will be inevitable for EBSD calibration methods, regardless of the choice of optimization algorithm. Besides, this systematic error depends on crystal orientation, as ED effect depends on the tilt angle of each Kikuchi band.

The aforementioned phenomena, *i.e.,* gray level reversal, non-uniform energy distribution and ED effect, can be included in dynamical simulations with specific simplification assumptions, and results in a better similitude with experimental EBSPs [25, 22]. The effect of a better similitude on EBSD indexation has recently been addressed, and a difference in PC calibration about 1% of EBSP width could exist [26]. However, only a few individual EBSPs have been analyzed, and the *accuracy* and *precision* of the indexed orientation are not addressed. The simulated EBSP of different crystal orientation or different acquisition condition requires lengthy and dedicated calculation, and cannot be efficiently projected from a pre-calculated master pattern. Besides, the complex theory of dynamical simulation and sizable coding works have limited its development to only a few groups, namely mostly those led by Winkelmann [27, 25, 22] and De Graef [28, 29].

The present work proposes to apply a weighted average to the simulated EBSPs in order to account for the effect of non-uniform electron energy, then rely on the IDIC framework to calibrate EBSD, including calibration of electron energy distribution, refinement of both Euler angles and PC position. Section 2 distinguishes the precision and accuracy of crystal orientation measurement, and stresses the importance of accuracy assessment. Section 3 introduces an IDIC algorithm for EBSD calibration that aims at retrieving electron energy distributions, crystal orientation and projection parameters. Section 4 analyzes high-resolution EBSPs of a single crystal Si wafer, and demonstrates the accuracy improvement of the algorithm. The application of energy weighting improves the similarity between experimental and simulated EBSPs and the accuracy of indexed Euler angles.

2 Precision and accuracy of EBSD indexation

When a quantity is measured from experiment, it is natural to inquire about its precision and accuracy. Ram *et al.* has provided a detailed comparison of these two notions [30]. The crystal orientation precision for Hough transform and dictionary approach has been assessed separately [30, 31].

Here, as defined by Ram *et al.*, the accuracy describes the distance between the measured value and the true value (the ground truth), and the precision is the standard deviation of several repeated measurements of the same physical object. The true crystal orientation is generally unknown, and as EBSD is the most commonly adopted technique to obtain crystal orientation, its measurement is often used as a reliable ground truth to characterize the accuracy of other measurement techniques [32]. One way to circumvent the absence of ground truth in accuracy assessment is to exploit the known sample features, such as twins in metallic samples. The measured misorientation across twin boundaries can be compared to the theoretical value, thus provide a metric of the accuracy. However, an error up to several degrees on each side of the twin boundary may hardly affect the apparent twin misorientation. Thus a favorable measurement of the latter is not a guaranty for an absolute precision of the indexation.

Figure 1a shows the inverse pole figure (IPF) map of a polycrystal Ni sample, which is provided by Wright *et*

al. [33] and shared with the community by Jackson *et al.*, including the indexation results by Hough transformation and dictionary indexation [34]. Many twin boundaries exist in the map, and a vertical profile across two boundaries is selected for misorientation analysis. Figure 1b plots the between-neighbor misorientation along the profile with three EBSD indexation algorithms: Hough indexation, dictionary indexation, IDIC EBSD indexation with floating or filtered PC values. As the Ni sample is not strained, between-neighbor misorientation could be attributed to indexation uncertainty. The former three indexation algorithms have comparable uncertainty levels around 0.40°, while the peak values reach 1.5°. The IDIC EBSD with filtered PC coordinates lead to the lowest uncertainty around 0.15°. Figure 1c-1d plot the misorientation to the central EBSP along the profile, with zooming on 60°, the theoretical misorientation across the FCC twin boundaries, and 0° respectively. Figure 1c shows that all 4 misorientation profiles fluctuate closely with the theoretical value, including those EBSPs that have between-neighbor as high as 1.5°. This phenomenon demonstrates that the relative misorientation across twin boundaries is not a sufficient proof of sub-degree EBSD indexation accuracy. Besides, the low uncertainty of IDIC EBSD indexation especially with filtered PC values is confirmed in Figures 1b-1d.

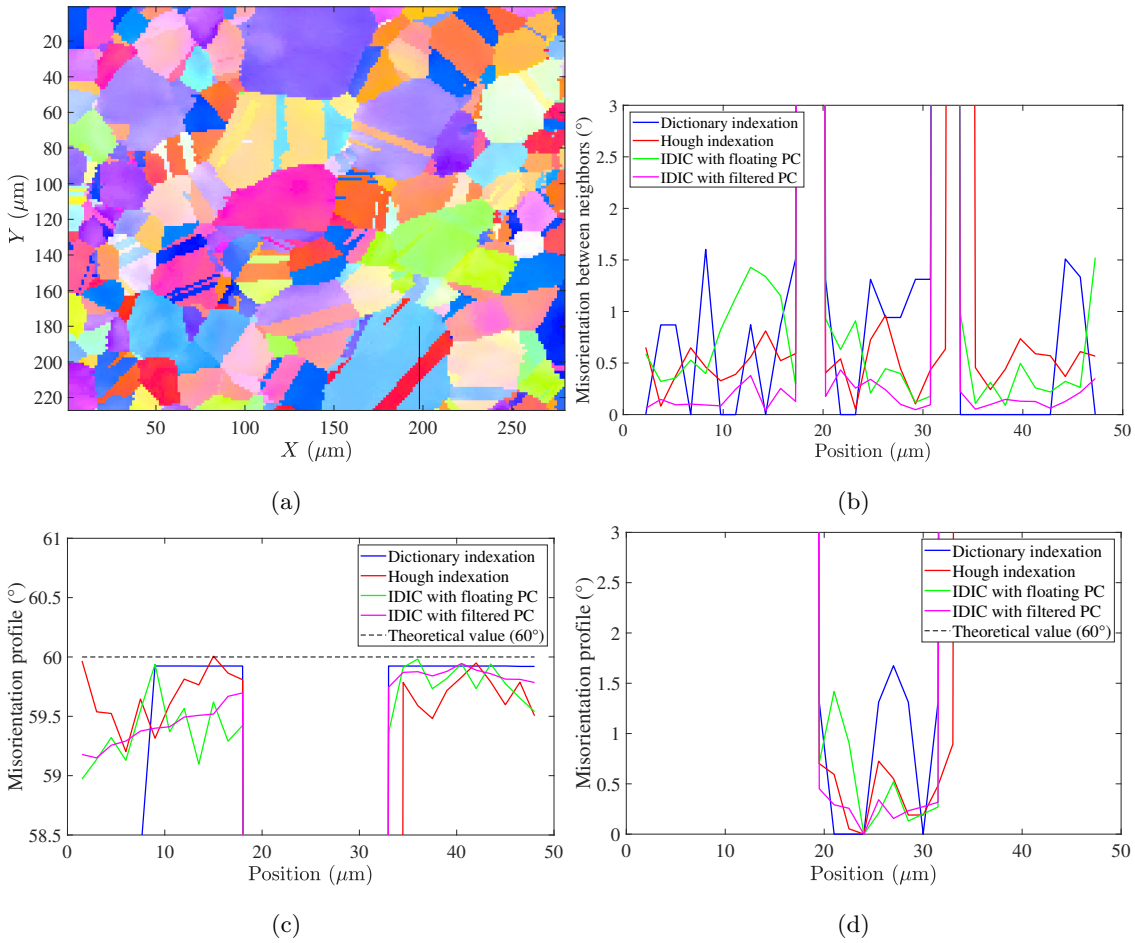

Figure 1: Analysis of misorientation across twin boundaries. (a) IPF map of a polycrystal Ni, where a black line marks the EBSPs across twin boundaries analyzed for misorientation; (b) Neighbor misorientation evaluated by different algorithms along the profile marked in (a); The misorientation between all EBSPs in the profile and an EBSP inside the red twin stripe is shown in (c) and (d), where the former focuses at 60° misorientation and the latter at 0°.

Another *accuracy* evaluation method is to use a standard sample with known crystal orientation to calibrate the EBSD system. It is vital to avoid or correct the experimental setup errors in this procedure, to name a few, the sample tilt angle, the misalignment of the tilt axis, the intentional or unintentional tilt of EBSD detector around different axes. These errors pose a severe threat on EBSD characterization, especially on the 'global optimization' approach of all EBSPs of an EBSD acquisition, which takes the EBSD geometry as a key input [15, 35]. There could exist unknown errors in all these aspects, and one remedy is to use the calibrated PC coordinates to correct all these potential sources of errors. To calibrate the sample surface plane more accurately, a large EBSD scan with high-definition EBSPs is preferred, the roughness of sample surface should be as low as possible, and ideally the sample should be unstrained, as the strain state influences the calibrated PC coordinates [11, 36, 18]. These requirements converge to a large-area EBSD scan with full definition on an unstrained single crystal sample, for example the single crystal Si wafer. The manufacturing of large high-purity Si wafer and its cut along a specific lattice plane is a mature technical question, thus it provides a cheap (the Si wafer piece used in this work costs 10

US dollars) but adequate standard sample to evaluate the accuracy of EBSD systems. Note that the uncertainty of Si wafer plane index is below 0.5°, as stated by most manufacturers.

3 EBSD calibration algorithm with a non-uniform BSE energy distribution

Integrated Digital Image Correlation (IDIC) has been introduced to measure *directly* and *optimally* the geometric transformation of interest (or parameters quantifying it) from image registrations. The projection geometry of EBSP is recalled in figure 2 together with the reference frame used in the paper.

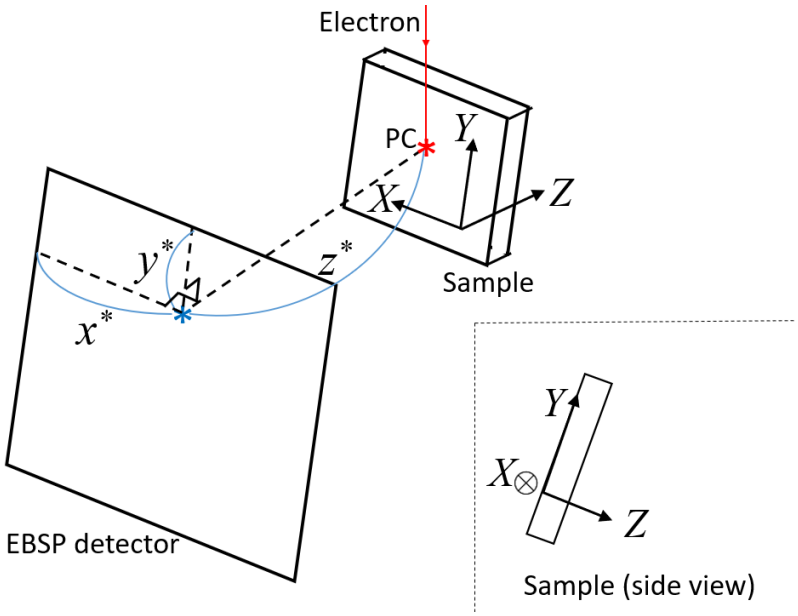

Figure 2: EBSD setup, with the projection center marked as a red star. The coordinate systems (x, y, z) associated to the EBSP detector and (X, Y, Z) associated to the sample are also defined here.

The IDIC EBSD algorithm is based on the assumption that only 6 projection parameters matter. Namely, the three coordinates of the projection center $\boldsymbol{x}^* = (x^*,\ y^*,\ z^*)$ and the three Euler angles $(\varphi_1, \phi, \varphi_2)$ of the crystal orientations which are collectively denoted as $\boldsymbol{P}$. In the present study, it is argued that several additional parameters are to be included in the calibration to account for the BSE energy distribution.

3.1 Monte-Carlo simulations

A way to study the energy distribution of BSEs is stochastic simulation such as Monte-Carlo methods. The software CASINO v2.5.1 [37] is used to simulate the interaction of 100,000 electrons of acceleration voltage 20 kV with a 70° tilted Si sample. The incident beam hits the sample at the calibrated PC coordinates, and the trajectories of BSEs inside the Si sample is shown in Figure 3a. The last segment of the trajectories are straightly prolonged until hitting the EBSD detector. The deviation angle α between the scattered BSE and the incident beam direction is also defined in Figure 3a. The relationships between scattering time, deviation angle and BSE energy are shown

in Figure 3b-d. A linear relationship exists between BSE energy loss and its scattering time inside the sample, as shown in Figure 3b. This is as anticipated, as more scattering times imply more inelastic collision and thus more energy losses. Figure 3c plots the data points of BSE scattering time and deviation angle, together with the mean profile and the errorbar. For BSE deviation angles lower than 60˚, the scattering time and BSE energy loss is also lower. Yet when the deviation angle reaches 60˚, the accompanying mean energy does not change.

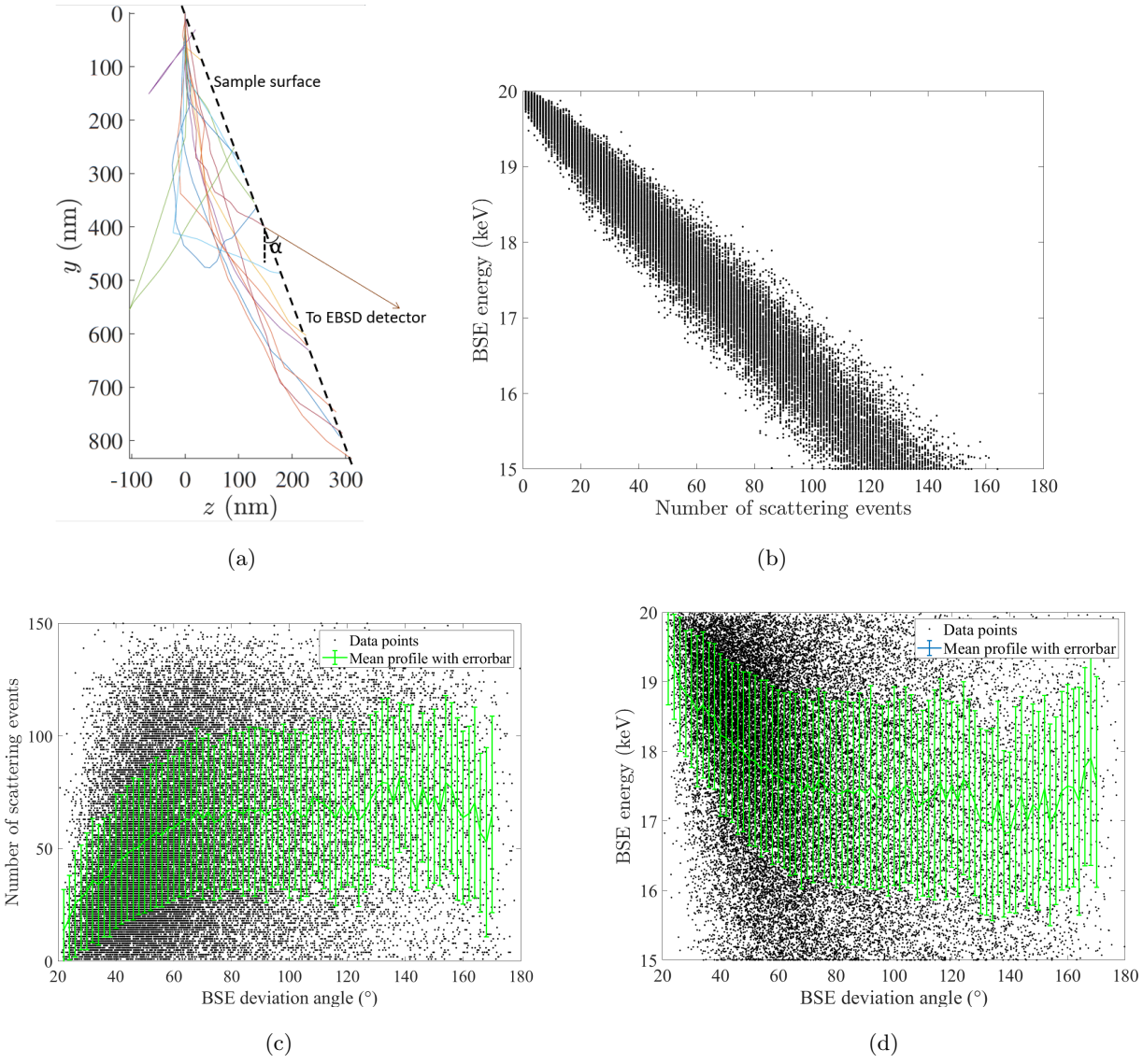

Figure 3: BSE energy analysis by Monte-Carlo simulation. (a) Examples of trajectories of BSEs inside the tilted sample, whose surface is marked with a dashed line; (b) The data points collecting the BSE energy and the number of scattering events inside Si sample. (c) The number of scattering events as a function of BSE deviation angle. (d) The BSE energy against the BSE deviation angle. The mean profiles and errorbar are plotted in (c) and (d).

The results of BSE energy distribution for EBSP are summarized in Figure 4. The locations of the hitting, plotted in Figure 4a, spread all over the detector with sufficient densities. The average energy distribution is shown in Figure 4b, and the energy at the bottom is 1 keV higher that at the top, a similar distribution as reported in

Ref. [23]. Not that the energy interval, 1.3 keV, is between the reported 2.5 keV in Ref [23] and 0.8 keV in Ref. [24].

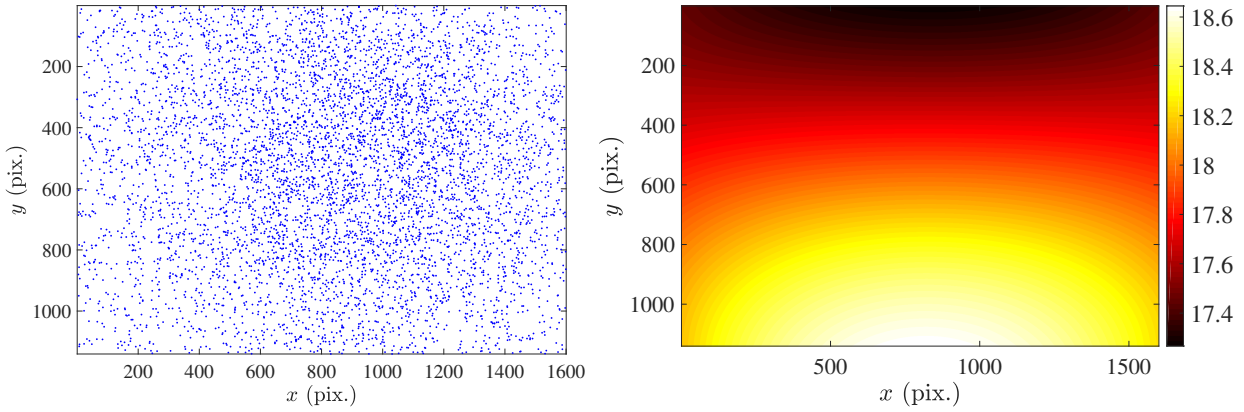

(a) (b)

Figure 4: Monte-Carlo simulation of the backscattered electrons. (a) The hitting point of BSEs on the EBSD detector; (b) The average electron energy field of the EBSP, $e(\boldsymbol{x})$, expressed in keV.

3.2 Accounting for energy distribution in EBSPs

Let $G(\boldsymbol{u}, e)$ be the dynamically simulated master pattern by EMsoft projected on the equatorial plane $\boldsymbol{u}$, as illustrated in Figure 5 for two values of BSE energy, $e = 16$ keV and 26 keV. Note that this large interval is chosen to highlight the Kikuchi band width differences.

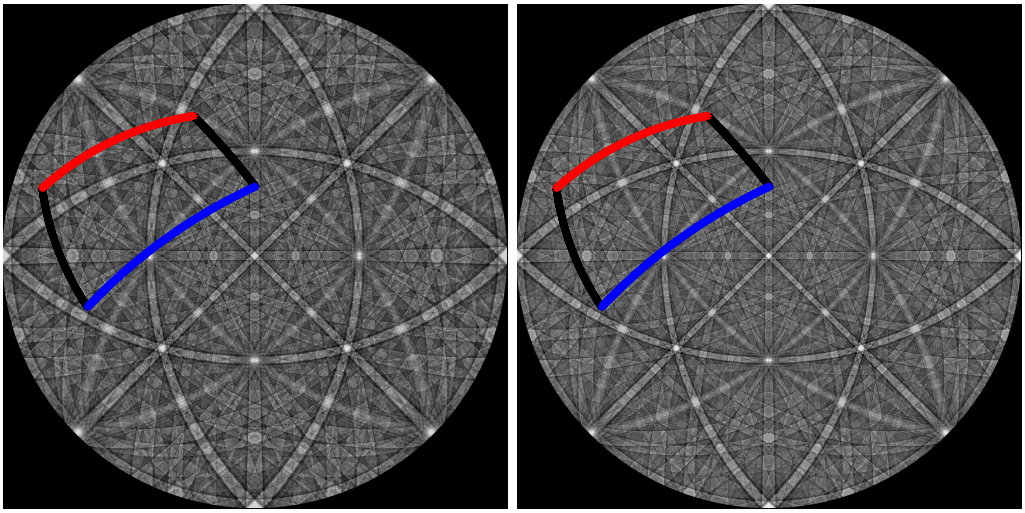

(a) (b)

Figure 5: Examples of $G(\boldsymbol{u}, e)$ for electron energy of $e = 16$ keV (a) and $e = 26$ keV (b) respectively. The selected region for projection, a function of projection parameters $\boldsymbol{P}$, is plotted in both figures. The Kikuchi bands are narrower for higher electron energies.

Without considering the energy distribution, the EBSP pattern is obtained by projecting the master pattern,

and is denoted $g(\boldsymbol{x}, \boldsymbol{P})$, with

$$g(\boldsymbol{x}, \boldsymbol{P}) = G(\boldsymbol{u}(\boldsymbol{x}, \boldsymbol{P}), e) \tag{1}$$

The Monte-Carlo simulations prompt one to account for the fact that the energy e should no longer be considered as a constant, but rather as a field. Hence the previous equation, Eq. 1, is generalized to

$$g(\boldsymbol{x}, \boldsymbol{P}) = G(\boldsymbol{u}(\boldsymbol{x}, \boldsymbol{P}), e(\boldsymbol{x})) \tag{2}$$

The selected region for projection, $\boldsymbol{u}(\boldsymbol{x}, \boldsymbol{P})$, is plotted on both patterns in Figure 5. Note that $\boldsymbol{u}$ does not depend on the BSE energy distribution by nature. This property helps the rapid construction of simulated EBSP of any energy distribution from the pre-calculated master patterns for a predetermined set of energies e_i, according to the following approximation

$$g(\boldsymbol{x}, \boldsymbol{P}) = \sum_i \eta_i(e(\boldsymbol{x})) G(\boldsymbol{u}(\boldsymbol{x}, \boldsymbol{P}), e_i) \tag{3}$$

where η_i are weights designed to allow for an interpolation of the patterns for any value of energy e. More precisely, if $e_i \leq e(\boldsymbol{x}) < e_{i+1}$, then

$$\begin{aligned} \eta_i &= \frac{(e_{i+1} - e(\boldsymbol{x}))}{(e_{i+1} - e_i)} \\ \eta_{i+1} &= \frac{(e(\boldsymbol{x}) - e_i)}{(e_{i+1} - e_i)} \end{aligned} \tag{4}$$

In the present study, the chosen energies are 17, 18, 19, 20, 21 keV, and the corresponding master patterns are calculated and stored beforehand, so that the final pattern can be obtained from the above weighted sum. It is acknowledged that this BSE energy modeling is a simplification of the real case, as in experimental EBSPs each pixel does not correspond to a single energy level, but rather a spectrum of continuous BSE energy levels. Nonetheless, the attribution of different BSE energy levels to an EBSP is already a progress in EBSD analysis. Note that $\eta_i(\boldsymbol{x})$ depends on the EBSD experimental setup, such as sample tilt angle and acceleration voltage.

In the analysis of the experimental EBSP, it is desirable not to impose a predetermined $e(\boldsymbol{x})$, but rather to evaluate it from the observed pattern. This task is basically out of reach without any further a priori information, because of the large number of unknowns, and the expected poor sensitivity. However, as shown in the energy distribution simulated by Monte-Carlo method, (Figure 4b) the spatial distribution of $e(\boldsymbol{x})$ is very regular [23], thus can be fitted by a low-order (such as 2nd order) polynomial to reduce the number of degrees of freedom in calibration. In the following, the BSE energy field $e(\boldsymbol{x}, \boldsymbol{E})$ is expressed as

$$e(\boldsymbol{x}, \boldsymbol{E}) = E_1 + E_2 x + E_3 y + E_4 x^2 + E_5 xy + E_6 y^2 \tag{5}$$

where $E_{1,2\ldots6}$ are collectively denoted as a vector $\boldsymbol{E}$, the BSE energy parameters. These parameters can be seen as supplementary to the classically considered ones $\boldsymbol{P}$. The inverse problem of determining the optimal $\boldsymbol{E}$ will be seen to be accessible. To summarize the above formulation, the simulated EBSP is written

$$g(\boldsymbol{x}, \boldsymbol{E}, \boldsymbol{P}) = \sum_i \eta_i(\boldsymbol{x}, \boldsymbol{E}) G(\boldsymbol{u}(\boldsymbol{x}, \boldsymbol{P}), e_i) \tag{6}$$

3.3 Formulation

Then a registration procedure similar to the IDIC algorithm described in Ref. [18] is proposed on the combined images with limited changes. To distinguish from the normal IDIC EBSD, the method described in the current paper is named as IDIC-E EBSD (Integrated Digital Image Correlation with Energy weighting).

The EBSP screen is chosen as the reference defining the (x, y) plane, or $z = 0$. The unit vector $\boldsymbol{w}$ linking the pattern center to each pixel $\boldsymbol{x} = (x, y, z = 0)$ of the screen can be expressed as

$$\boldsymbol{w} = \frac{(\boldsymbol{x} - \boldsymbol{x}^*)}{|\boldsymbol{x} - \boldsymbol{x}^*|} \tag{7}$$

In order to rotate this vector from the screen frame of reference $\boldsymbol{w}$ to that of the spherical master pattern, $\boldsymbol{v}$, one should multiply it by a rotation operator $\boldsymbol{Q}$

$$\boldsymbol{v} = \boldsymbol{Q}\boldsymbol{w} \tag{8}$$

whose expression, using the Euler angles, reads in Bunge notations:

$$\boldsymbol{Q} = \begin{bmatrix} \cos\varphi_1 \cos\varphi_2 - \sin\varphi_1 \sin\varphi_2 \cos\phi & \sin\varphi_1 \cos\varphi_2 + \cos\varphi_1 \sin\varphi_2 \cos\phi & \sin\varphi_2 \sin\phi \\ -\cos\varphi_1 \sin\varphi_2 - \sin\varphi_1 \cos\varphi_2 \cos\phi & -\sin\varphi_1 \sin\varphi_2 + \cos\varphi_1 \cos\varphi_2 \cos\phi & \cos\varphi_2 \sin\phi \\ \sin\varphi_1 \sin\phi & -\cos\varphi_1 \sin\phi & \cos\phi \end{bmatrix} \tag{9}$$

The spherical projection of $\boldsymbol{v}$ onto the master pattern plane, $\boldsymbol{u}$, is written

$$\boldsymbol{u} = \frac{\boldsymbol{v} - \boldsymbol{n}}{(1 - \boldsymbol{v}.\boldsymbol{n})} + \boldsymbol{n} \tag{10}$$

where $\boldsymbol{n} = (0, 0, 1)^\top$ denotes the unit vector pointing at the north pole. Thus the projected position, $\boldsymbol{u}(\boldsymbol{x})$, on the master pattern can be expressed explicitly as a function of $\boldsymbol{x}$ and of the projection parameters $\boldsymbol{P} = (\varphi_1, \phi, \varphi_2, x^*, y^*, z^*)$.

3.4 Optimization

In the IDIC-E EBSD algorithm, experimental EBSP is taken as $f(\boldsymbol{x})$. The dynamical simulation of the EBSP master pattern for the i^{th} energy level is $G_i(\boldsymbol{x}, \boldsymbol{P})$. The algorithm involves matching at best $f(\boldsymbol{x})$ and $g(\boldsymbol{x}, \boldsymbol{E}, \boldsymbol{P})$, through the minimization of a quadratic norm of the residual r summed over the entire ROI. The cost function to minimize is written

$$\Theta = \sum_{ROI} \omega(\boldsymbol{x})^2 \left[f(\boldsymbol{x}) - g(\boldsymbol{x}, \boldsymbol{E}, \boldsymbol{P}) \right]^2 \tag{11}$$

where $\omega(\boldsymbol{x})$ is the weight associated to each pixel $\boldsymbol{x}$, $g_{\boldsymbol{u}}(\boldsymbol{x}, \boldsymbol{E}, \boldsymbol{P})$ is the current estimate of simulated EBSP during iterative algorithms. The weights ω are introduced here as they may be used to make this functional *optimal* with respect to the handling of noise. The minimization of the cost function leads to successive corrections of the transformation $\boldsymbol{u}(\boldsymbol{x})$ or $\eta(\boldsymbol{x}, \boldsymbol{E})$ estimation until convergence [38]. Starting from an approximate solution, the transformation $\boldsymbol{u}(\boldsymbol{x}, \boldsymbol{P})$ and $\eta(\boldsymbol{x}, \boldsymbol{E})$ are progressively corrected with linear combinations of sensitivity fields constituting the kinematic basis. The cost function (11) is alternatively minimized by optimizing $\boldsymbol{P}$ and $\boldsymbol{E}$, each of which consists of iterative minimization with a Gauss-Newton algorithm.

A slight modification of any parameter δP_j with given energy parameters $\boldsymbol{E}$, induces a modification of the corrected deformed image as

$$\begin{aligned} \delta g(\boldsymbol{x},\boldsymbol{E},\boldsymbol{P})\big|_{\boldsymbol{E}} &= \sum_j \sum_i \eta_i(\boldsymbol{x},\boldsymbol{E}) \nabla_{\boldsymbol{u}} G(\boldsymbol{u},e_i) \cdot \frac{\partial \boldsymbol{u}(\boldsymbol{x},\boldsymbol{P})}{\partial P_j} \delta P_j \\ &\equiv \sum_j \Phi_j(\boldsymbol{x},\boldsymbol{E},\boldsymbol{P}) \delta P_j \end{aligned} \tag{12}$$

where Φ_j is a compact notation for the sensitivity with respect to parameter P_j. The column vector $\{\boldsymbol{\delta P}\}$ gathering all corrections to $\boldsymbol{P}$ is obtained from the linear system

$$[\boldsymbol{M}]\,\{\boldsymbol{\delta P}\} = \{\boldsymbol{\gamma}\} \tag{13}$$

where $[\boldsymbol{M}]$ is the Hessian matrix of size 6×6 at iteration $n-1$ in $\boldsymbol{P}$ optimization.

$$M_{jk}^{(n-1)} = \sum_{ROI} \omega(\boldsymbol{x})^2 \left[\Phi_j(\boldsymbol{x},\boldsymbol{E},\boldsymbol{P})\right] \left[\Phi_k(\boldsymbol{x},\boldsymbol{E},\boldsymbol{P})\right] \tag{14}$$

and the second member $\{\boldsymbol{\gamma}_j\}$ includes the residual field in $\boldsymbol{P}$ optimization.

$$\gamma_j^{(n)} = \sum_{ROI} \omega(\boldsymbol{x})^2 \left(f(\boldsymbol{x}) - \widetilde{g}^{(n)}(\boldsymbol{x},\boldsymbol{E},\boldsymbol{P})\right) \Phi_j(\boldsymbol{x},\boldsymbol{E},\boldsymbol{P}) \tag{15}$$

When $\|\{\boldsymbol{\delta P}\}\| < \epsilon_P$, ϵ_P being chosen equal to 10^{-6} for all the calculations of this paper, the minimization stops and $\boldsymbol{P}$ is stored. Otherwise, $\boldsymbol{P}$ is updated

$$\boldsymbol{P}^{(n)} = \boldsymbol{P}^{(n-1)} + \boldsymbol{\delta P}^{(n)} \tag{16}$$

Once $\boldsymbol{P}$ is obtained, the simulated EBSP, with the prescribed BSE energy field, resembles the reference experimental EBSP at best.

A similar IDIC procedure could be designed to calibrate the BSE energy field. The sensitivity vector of $g(\boldsymbol{x},\boldsymbol{E},\boldsymbol{P})$ with any energy parameter E_j with given projection parameters $\boldsymbol{P}$, is denoted $\Psi_j(\boldsymbol{x})$

$$\begin{aligned} \delta g(\boldsymbol{x},\boldsymbol{E},\boldsymbol{P})\big|_{\boldsymbol{P}} &= \sum_j \sum_i G(\boldsymbol{u},e_i) \frac{\partial \eta_i(e)}{\partial e} \frac{\partial e(\boldsymbol{x})}{\partial E_j} \delta E_j \\ &\equiv \sum_j \Psi_j(\boldsymbol{x},\boldsymbol{E},\boldsymbol{P}) \delta E_j \end{aligned} \tag{17}$$

The column vector $\{\boldsymbol{\delta E}\}$ gathering all corrections to $\boldsymbol{E}$ is obtained

$$[\boldsymbol{N}]\,\{\boldsymbol{\delta E}\} = \{\boldsymbol{\kappa}\} \tag{18}$$

where $[\boldsymbol{N}]$ is the Hessian matrix at iteration $n-1$

$$N_{jk}^{(n-1)} = \sum_{ROI} \omega(\boldsymbol{x})^2 \Psi_j(\boldsymbol{x},\boldsymbol{E},\boldsymbol{P}) \Psi_k(\boldsymbol{x},\boldsymbol{E},\boldsymbol{P}) \tag{19}$$

and the second member $\{\boldsymbol{\kappa}_j\}$ in $\boldsymbol{E}$ optimization,

$$\kappa_j^{(n)} = \sum_{ROI} \omega(\boldsymbol{x})^2 \left(f(\boldsymbol{x}) - \widetilde{g}^{(n)}(\boldsymbol{x},\boldsymbol{E},\boldsymbol{P})\right) \Psi_j(\boldsymbol{x},\boldsymbol{E},\boldsymbol{P}) \tag{20}$$

The determination of $\boldsymbol{\delta E}^{(n)}$ allows to update $\boldsymbol{E}$ as

$$\boldsymbol{E}^{(n)} = \boldsymbol{E}^{(n-1)} + \boldsymbol{\delta E}^{(n)} \tag{21}$$

The same stopping condition for $\boldsymbol{E}$ optimization is adopted, though the convergence criteria ϵ_E is set to 10^{-4}. The above detailed IDIC-E algorithm is summarized in the flowchart shown in Figure 6a.

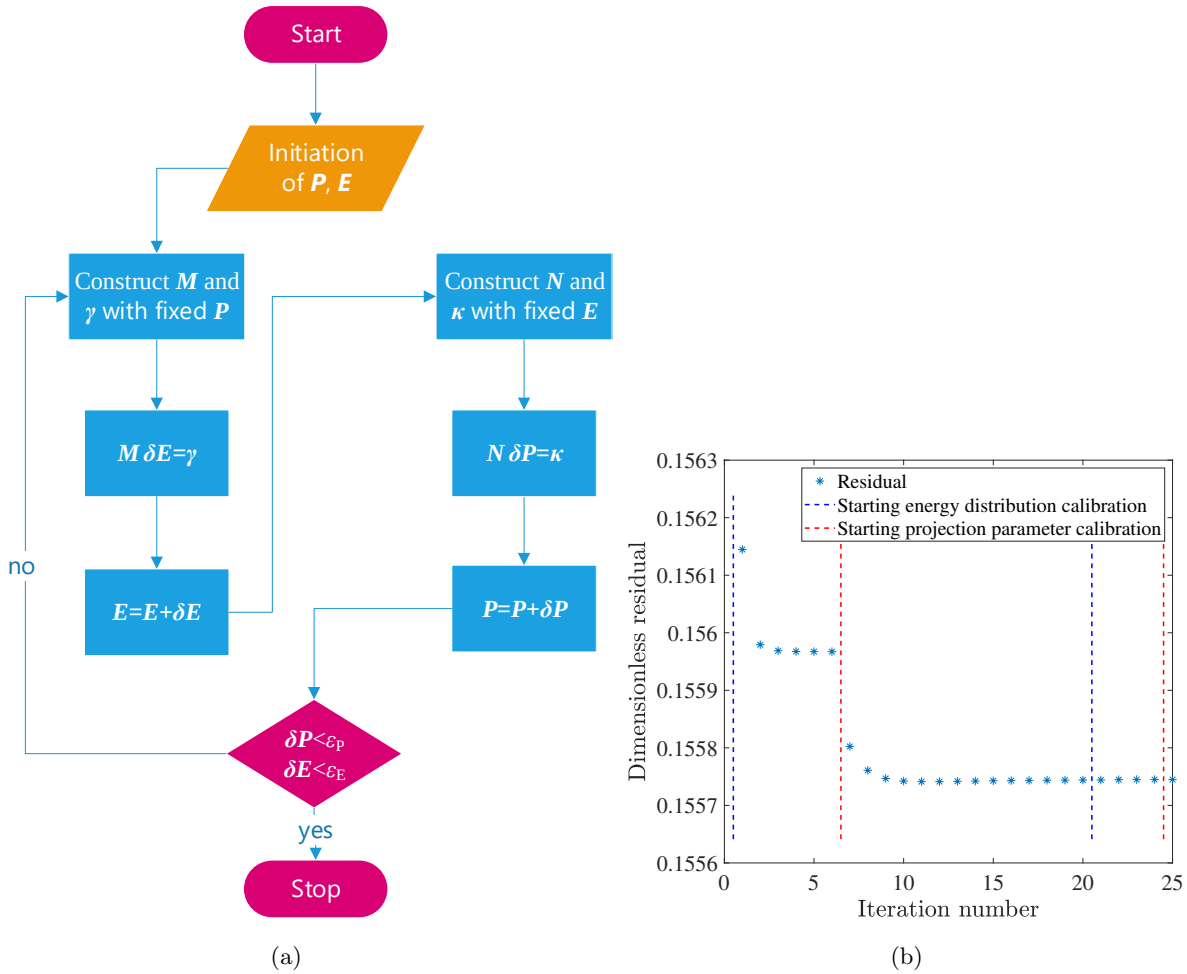

Figure 6: (a) Flowchart of the IDIC-E algorithm. (b) The evolution of the cost function Θ during the IDIC-E EBSD calibration of an EBSP of Si wafer.

Generally, only a few outer iterations are necessary in IDIC-E EBSD before convergence as shown in Figure 6b, as the crystal orientations and projection center values given by single-energy IDIC EBSD are already close enough to the IDIC-E EBSD results. Besides, the cost function Θ drops both in $\boldsymbol{E}$ calibration and $\boldsymbol{P}$ calibration, stressing the necessity to include all these parameters into the EBSD analysis.

Figure 7a shows the energy field calibrated by IDIC-E EBSD, and the corresponding energy weights are given in Figure 7(b-d).

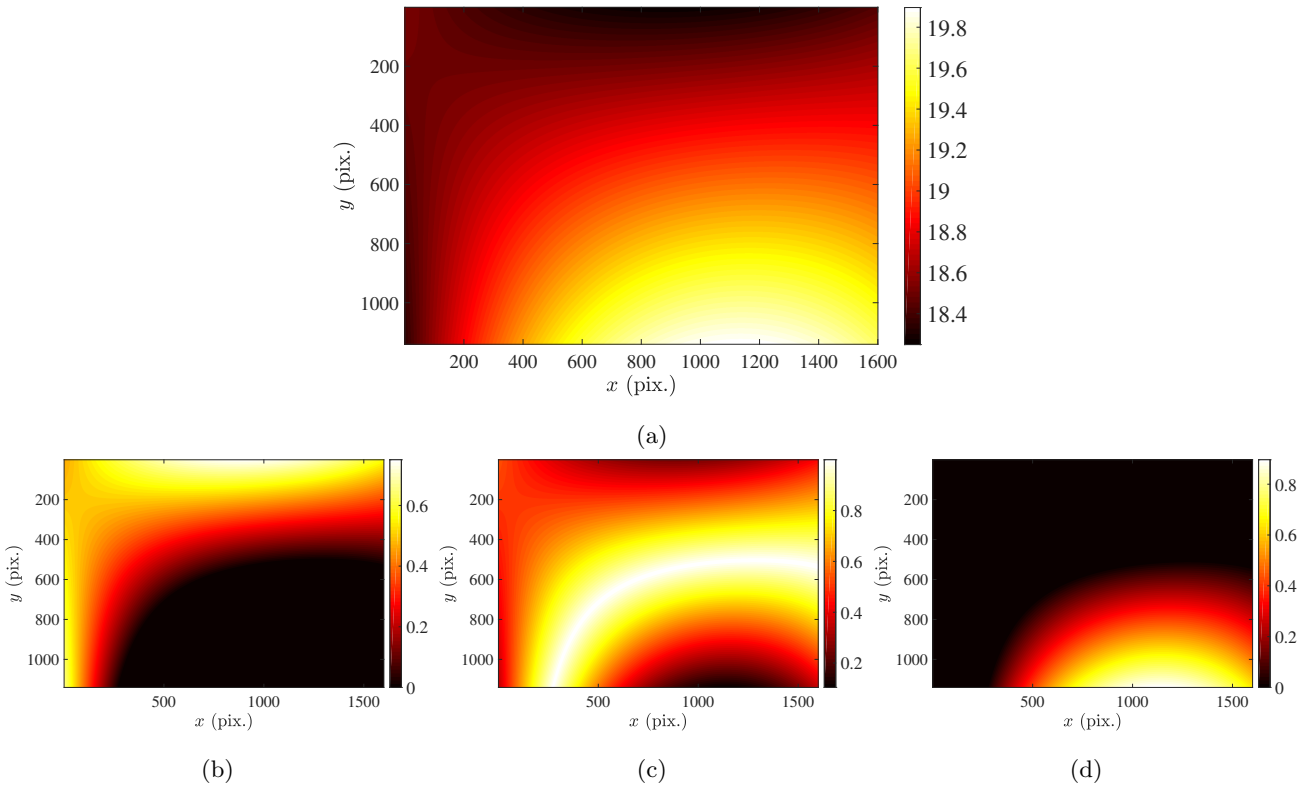

Figure 7: Examples of η fields, the weighting ratio defined at each EBSP pixel, for EBSD analysis with considerations of BSE energy. (a) Mean energy of scattered electrons in the detector, $e(\boldsymbol{x})$; (b-d) η weight fields for master patterns of 18, 19 and 20 keV respectively in IDIC-E EBSD calibrated BSE energy model.

The above energy field $e(\boldsymbol{x})$ as obtained from IDIC-E EBSD, can be compared to one simulated by CASINO (Figure 8. The latter energy field has been generated with the same code and parameters as the one shown in Figure 4b. Their only difference is the deliberately introduced alignment error that will be explained in Section 4. The simulated energy field with tilt is comparable with the calibrated one, though a difference of about 1kV exist between them. This 1kV contrast is presumably due to the gray level profiles across Kikuchi bands, such as the excess-deficiency effect or the smooth gray level transition at band edges, not perfectly simulated in dynamical simulations. Nevertheless, this similarity validates the proposed IDIC-E EBSD methodology.

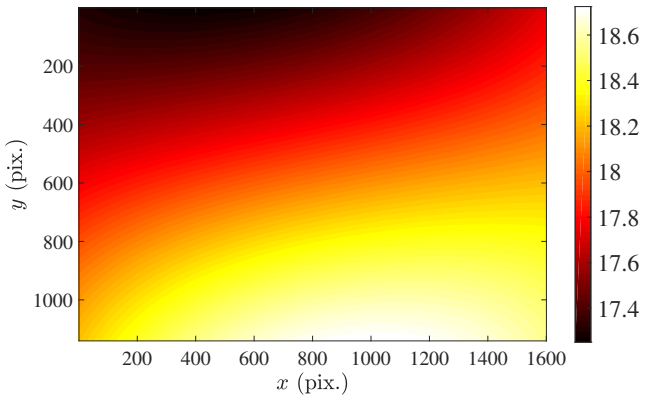

Figure 8: An example of Monte-Carlo simulation of the energy field obtained after tilting the Si wafer sample to mimic a possible imperfect set-up.

4 Improved indexation accuracy of a Si wafer

The EBSD dataset of a commercial Si wafer, first reported in Ref.[39], is used again to characterize the accuracy of IDIC and IDIC-E indexation. The sample does not show regular engravings on its surface. No strain is introduced in the sample, thus the local misorientation is expected to be negligible. The sample is observed in Tescan MIRA3 scanning electron microscope via the Bruker EBSD technique, with an acceleration voltage 20kV and beam current 10nA. The sample is placed in the chamber using a stub pre-tilted at 70°. In order to limit the charging effect, a large piece of copper conductive tape is 'sandwiched' between the wafer and the EBSD stage. No alignment of the wafer surface by rotation was achieved due to the lack of regular marking on the surface. The step size is deliberately set to a very large value, 50 µm, as the Si wafer lacks fine structures. A total of 1200 high-resolution (1140×1600 pixels) diffraction patterns are recorded using a Bruker e$^-$Flash^{HD} EBSD detector, covering an nominal area of 1.5×2 mm^2.

An example of high quality experimental EBSP of Si wafer is shown in Figure 9a. The Si master patterns of 17, 18, 19, 20 and 21 kV simulated by EMsoft, selectively shown in Figure 5, are used for the IDIC EBSD indexation. A simulated EBSP is shown in Figure 9b, whose residual compared with the experimental EBSP is shown in Figure 9c. The simulated EBSP successfully predicts the position and width of Kikuchi bands, but the intensity distribution is not fully captured, as repetitively stated before [40, 41]. Besides, the noise level in the experimental EBSP is not negligible, and the weighting field ω obtained by inverting the second-order polynomial fitting of the standard noise deviation is shown in Figure 9d. Here ω is higher in the center-left area, which coincides with the very bright Kikuchi bands shown in Figure 9a.

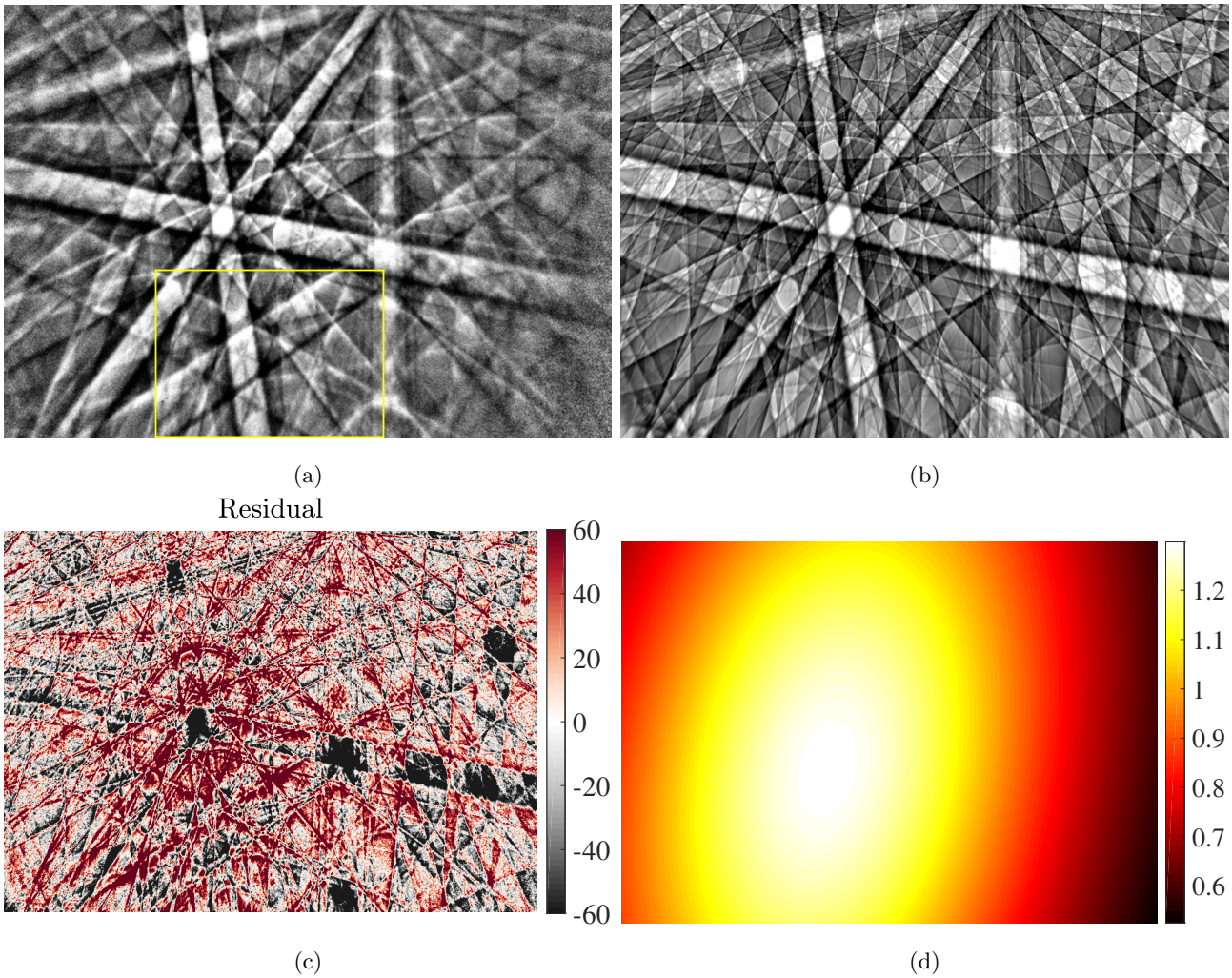

Figure 9: (a) Experimental EBSP of the single crystal Si wafer. (b) The numerical EBSP projected from the master pattern. (c) Residual between (a) and (b). (d) Weights of EBSP ω used in IDIC EBSD indexation.

The effect of considering energy distribution on EBSP is illustrated in Figure 10. An enlargement of the highlighted region shown in Figure 9a is shown in Figure 10a. The simulated EBSPs of BSE energy 18 keV, 19keV, 20keV and 21keV are shown in Figures 10b,c,e,f respectively. As the BSE energy increases, a black trough appears and widens, stretching from the lower-left to the upper-right. After the IDIC-E EBSD calibration, the energy field is calibrated, and a combined EBSP is generated as shown in Figure 10d. Though Figure 10d is obtained by combining several single-energy simulated EBSPs (Figure 10bcef), Figure 10d is more similar to the experimental EBSP than any of the four Figures 10bcef. This test case shows the benefit of BSE energy calibration in EBSD analysis. Previous works have made this whole-figure comparison of experimental and simulated EBSPs of various electron energy levels [42], or gets the energy distribution for a single Kikuchi band [23], yet the current paper shows that the different mono-energy EBSPs intertwine to reproduce the observed one.

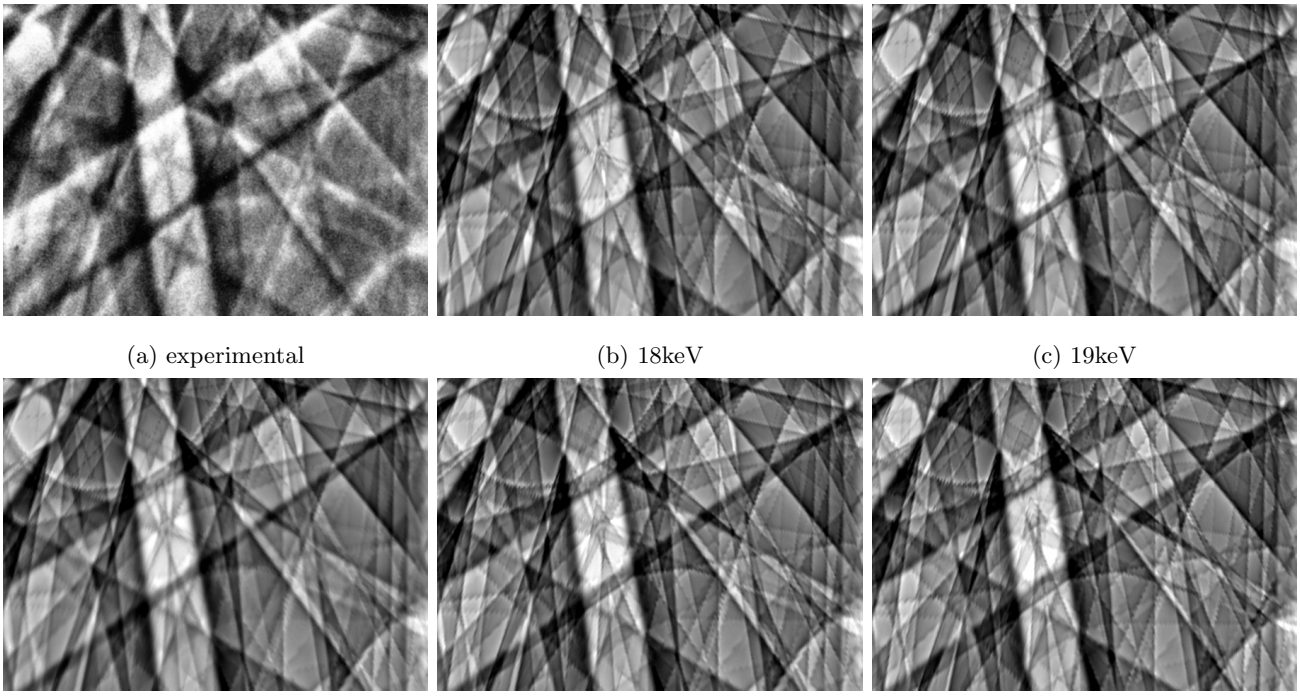

(a) experimental (b) 18keV (c) 19keV

(d) simulated (e) 20keV (f) 21keV

Figure 10: Comparison of experimental EBSP and a series of simulated EBSPs of different energy levels. (a) Zoomed experimental EBSP of the single crystal Si wafer. The numerical EBSP projected from the 18 kV master pattern (b), 19 kV pattern (c), 20 kV pattern (e) and 21 kV pattern (f). (d) corresponds to the simulated EBSP with IDIC-E calibrated energy distribution fields. Readers are invited to compare the black trough stretching from the lower-left to the upper-right of all figures.

Si or Ge single crystal has frequently been used for testing EBSD calibration methods [43, 44, 19, 16]. Alkorta *et al.* [44] have compared the normal of fitted plane for different positions of Si single crystal, yet their precision is of order 1°, and the calibrated Euler angles are not verified by the [001] sample surface. When one aims at assessing the *accuracy* of EBSD indexation, the 'ground truth' must be reliably known. However, the true orientation is mostly unknown. The crystal plane of Si single crystal wafer is known precisely thanks to the surface energy minimization, yet the uncertainty of experimental setup of EBSD, such as sample tilt angle and the positioning of EBSP detector add to the error of the true crystal orientation. In this case, one could rely on the fitting results of calibrated PC fields to get the ground truth. We hereby propose the following procedure to quantify the crystal orientation accuracy and PC coordinates accuracy based on the Si wafer of known cutting surface:

1. Calibrate all the crystal orientations $(\varphi_1, \phi, \varphi_2)$ and projection centers of EBSPs acquired in the 2D EBSD test.

2. Apply a plane fitting based on the PC point cloud, to get the surface normal $\boldsymbol{N}_s$ of the sample.

3. Based on the known Si wafer surface lattice index $\boldsymbol{s} = [0, 0, 1]^\top$, apply the rotation matrix $\boldsymbol{Q}$ corresponding

to $(\varphi_1, \phi, \varphi_2)$ to obtain the rotated surface lattice index $\boldsymbol{S}_r$,

$$\boldsymbol{S}_r = \boldsymbol{Q}\boldsymbol{S} \tag{22}$$

Note that the explicit expression of $\boldsymbol{Q}$ is provided in Equation 9. The misorientation between vectors $\boldsymbol{S}_r$ and $\boldsymbol{N}_s$, $\arccos(\boldsymbol{S}_r \cdot \boldsymbol{N}_s)$, is a metric of the *orientation discrepancy* between the indexed orientation and the nominal orientation. This discrepancy comprises of 2 parts: the error of the crystal orientation indexation and the error of Si wafer cutting along the wanted plane. In fact, a full 2D orientation discrepancy map can be drawn this way.

It is important to note that Equation 22 holds true because the crystal orientation is defined as the rotation from the EBSD detector to the crystal lattice in IDIC EBSD, rather than the rotation from the sample coordinates to the crystal lattice.

All the 1200 EBSPs are analyzed by our in-house IDIC EBSD and the current IDIC-E EBSD calibration methods, and the resulting pattern center coordinates are shown in Figures 11a-11c respectively. An interesting point is that while the x^* field varies along the X direction, the gradient of y^* and z^* fields are not along Y. This effect is not due to the charging effect, which would also influence x^*. In fact, this is due to the bad alignment of sample surface and the EBSD scanning direction. PC coordinate shifts between IDIC EBSD and IDIC-E EBSD are shown in Figures 11d-11f. PC values are shifted less than 1 pixel when the BSE energy distribution is considered in the calculation, and y^* has a most significant upward shift, resulting from the fact that BSE energy inhomogeneity mainly exist in the y direction. Figure 11g shows the misorientation between the calibration results of IDIC and IDIC-E. This orientation discrepancy level, up to 0.05°, several times higher than the reported uncertainties of FPM indexation, shows that the systematic errors of calibration results are non-negligible. Pattern center data for this large-field EBSD acquisition provide valuable information about the sample surface geometry.

As the single crystal Si wafer is unstrained, its surface is assumed strictly planar. Thus, a plane fit is applied to the PC data clouds, minimizing

$$T(\boldsymbol{n}, d) = (\boldsymbol{x}^* \cdot \boldsymbol{n} - d)^2 \tag{23}$$

The vector $\boldsymbol{n}$ from the planar fitting is the normal to the plane in the reference of EBSD detector, which is evaluated to $(0.4025\ 0.1779\ 0.8979)^\top$ by IDIC-E EBSD. Note that this direction is 25.2° from the nominal vector $(0, \cos(70°), \sin(70°))^\top$. This large misorientation, originated from the difficulty to align the 5 cm-wide wafer without regular marking on the surface correctly in EBSD position, does not compromise the EBSD analysis as long as the inclination error is corrected by the planar fitting. Besides, the mis-positioning of the Si wafer causes directly the tilt in BSE energy fields shown in Figure 8.

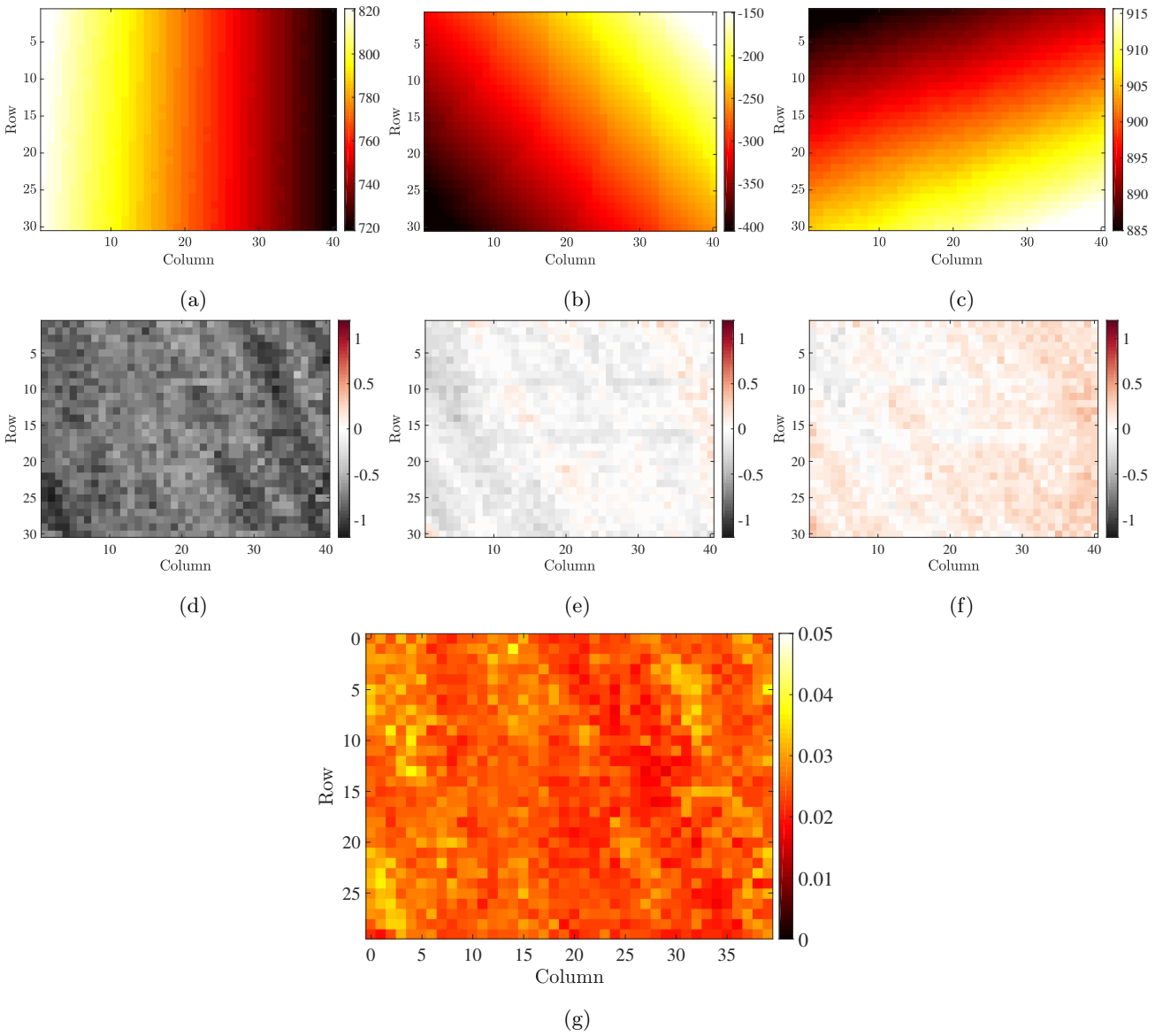

Figure 11: Results of IDIC-E EBSD calibration on Si wafer. Retrieved pattern center coordinates x^* (a), y^* (b) and z^* (c) by IDIC-E EBSD. The definition of these coordinates is given in Figure 2. (d-f) Pattern center coordinate shifts (in pixels) between IDIC EBSD and IDIC-E EBSD. (g) The misorientation (in °) map between IDIC and IDIC-E indexation.

As the 1200 EBSPs are generated with the same EBSD set-up, the BSE energy fields should be constant. The mean value and variability of the 1200 BSE energy fields calibrated by IDIC-E EBSD are shown in Figure 12. The tilt of energy field is preserved in the mean field shown in Figure 12a. The median of the standard deviation field is 0.05 keV, though the variability of calibrated BSE energy is higher at the corners (especially the right-bottom one). This is due to the polynomial fitting of energy field $e(\boldsymbol{x})$ tends to have higher residuals at end data (as for other polynomial fittings). This consistency of BSE energy calibration demonstrates the robustness of the proposed method.

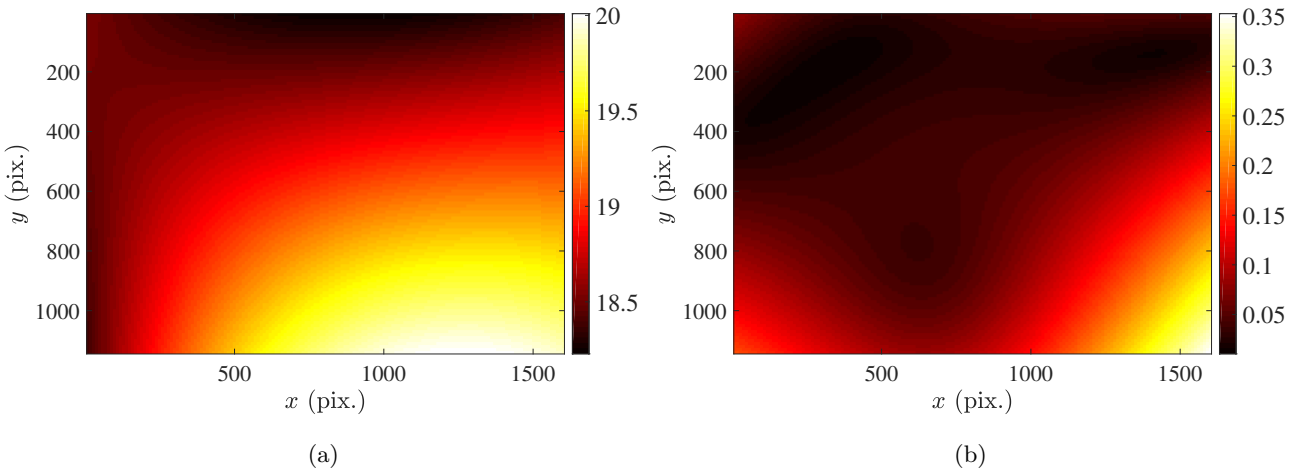

Figure 12: The mean field (a) and standard deviation field (b), both expressed in keV, of BSE energy calibrated by IDIC-E EBSD.

The distance of the calibrated PC point cloud to the fitted plane has a standard deviation of 0.187 pixel, or roughly 10^{-4} of EBSP width, which can be interpreted as the uncertainty of the PC calibration. These results show that the IDIC EBSD calibration helps to quantify the sample position relative to the EBSD detector and correct any slight mispositioning of EBSD analyses. Knowing the sample position, such as sample-to-detector distance, sample tilt angle and tilt axis, is of vital importance in advanced EBSD analyses, such as elastic strain measurement by HR-EBSD [36, 44] and the lattice constant measurement [45]. Several methods have been proposed to answer this need. Plancher *et al.* [46] used a specific sample holder designed to precisely position the sample and calibrate scanning parameters, by imaging a supplementary Si grid parallel to the stage reference plane. Thanks to the precision of IDIC EBSD calibration, the geometrical parameters can now be obtained by only imaging the sample itself.

Figure 13 plots the different BSE energy models used in this study and their corresponding crystal orientation indexation error. Three BSE energy models are adopted, namely a uniform 19 keV BSE energy field shown in Figure 13a, a linear stratified energy distribution between 18 and 20 keV shown in Figure 13b and the calibrated BSE energy distribution by IDIC-E EBSD shown in Figure 13c. Note that most existing EBSD indexation software packages assume a uniform BSE energy distribution [1, 18]. The estimated indexed crystal orientation error fields are shown in Figures 13d-f, corresponding to the three BSE energy fields respectively. The histogram profiles of the three orientation contrast fields are plotted in Figure 13g. The median crystal orientation discrepancy is 0.350° for the uniform 19 keV energy model, 0.250° for the linear 18-20 keV energy model and 0.222° for the IDIC-E calibrated energy model. The remaining crystal orientation contrast could be attributed to the imperfect Si wafer (non-zero misorientation between the sample surface and [001] direction), and other systematic errors causing inaccuracy in EBSD calibration, such as the optical distortion in EBSD detector or excess-deficiency effect. The overall reduction of crystal orientation error demonstrates the improvement of crystal orientation indexation when BSE energy distribution is considered.

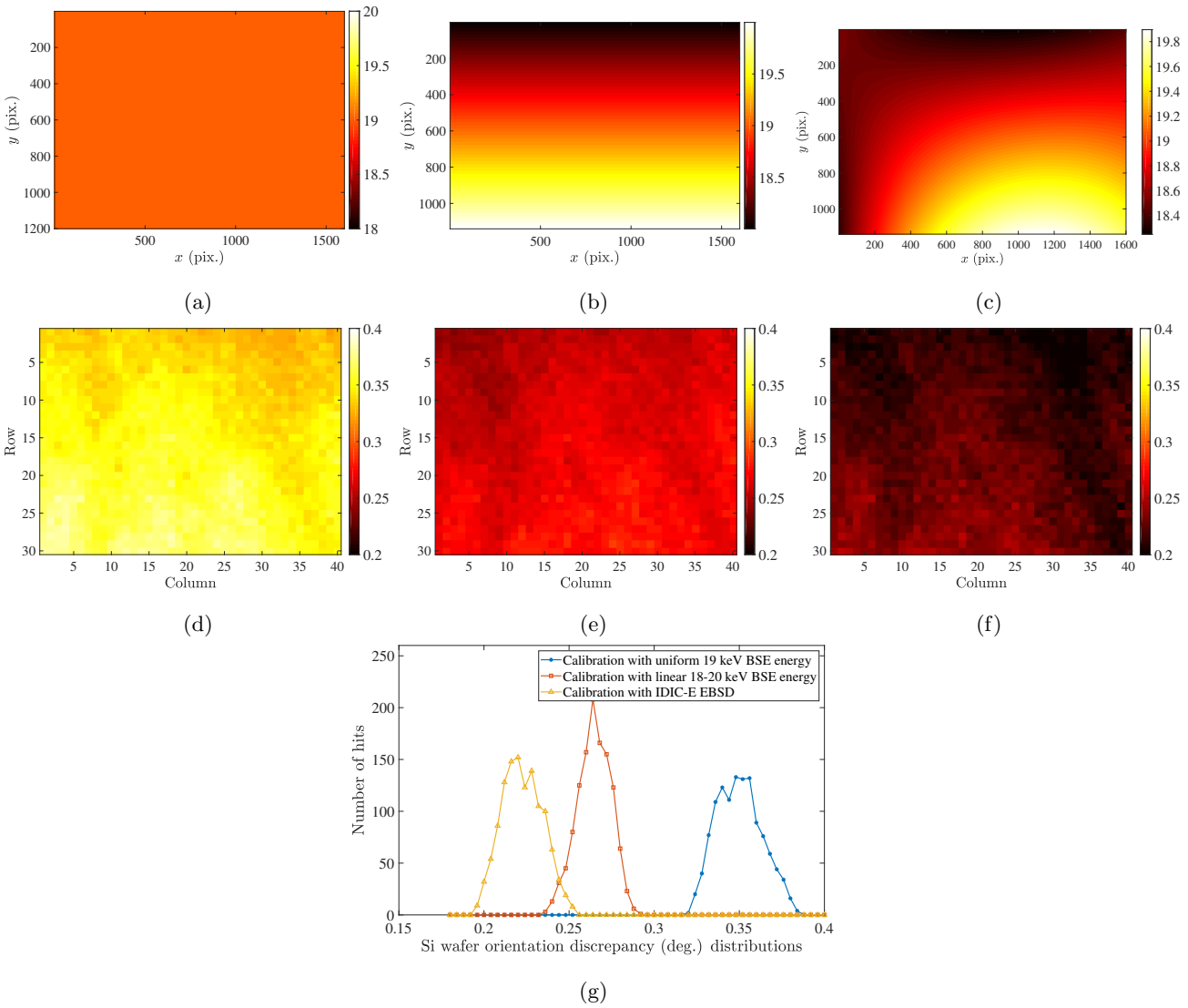

Figure 13: Crystal orientation discrepancy of Si wafer based on different BSE energy distributions. (a-c) BSE energy (in keV) distribution models used in IDIC EBSD calibration. (a) a uniform 19 keV BSE energy field. (b) Linear and stratified energy distribution between 18 and 20 keV. (c) The calibrated BSE energy field by IDIC-E EBSD. (d-f) show the orientation discrepancy (in °) for BSE energy fields (a-c) respectively. (g) plots the histogram profiles of (d-f).

To sum up, the IDIC EBSD calibration on 1140×1600-pixel large step-size EBSD acquisition on Si single crystal wafer has an uncertainty in PC calibration of 0.187 pixel, and median crystal orientation discrepancy of 0.222°. The accuracy of IDIC-E indexation is deemed improved as the orientation discrepancy is effectively reduced, as compared to the result (0.350°) with a homogeneous energy distribution. Another proof is the continuous reduction of cost function Θ when the BSE energy distribution is considered.

5 Conclusion

Full pattern match with simulated diffraction pattern has drawn increasing attention in advanced EBSD analyses, mainly thanks to its high precision. Some aspects of experimental EBSPs are however difficult or costly to simulate, such as Kikuchi band brightness asymmetry, gray level reversal for small tilt angles and non uniform diffracted electron energy. This paper proposes to overcome the inhomogeneous energy obstacle by relying on a dedicated integrated digital image correlation algorithm that quantifies the electron energy distribution *and* projection parameters.

Precision, or uncertainty of EBSD crystal orientation indexation has been frequently addressed, yet its correctness, or accuracy, is seldom analyzed, as the ground truth of crystal orientation is generally unknown. In this paper the (100)-face single crystal Si wafer is used as a standard sample to calibrate the EBSD system. By a large-area (2×1.5 mm^2) high definition (1140×1600) EBSD acquisition and analyzing full field projection center values, the sample surface inclination relative to the EBSD detector is precisely calibrated, thus the error of sample tilt and EBSD detector tilt are corrected in the accuracy assessment. As a result, the contrast between EBSD-indexed orientation and manufacturer-indicated orientation is assessed precisely.

By considering the inhomogeneous electron energy distribution of EBSPs, the orientation contrast has improved by 0.128° as demonstrated in the Si wafer dataset. Failing to account for the energy distribution effect induce a deviation of the PC by near 1 pixels, especially for y^*. The remaining crystal orientation contrast, estimated around 0.222° for the Si wafer, could be attributed to other effects, such as Si wafer cutting error, Kikuchi band brightness asymmetry and optical distortion of EBSD detector. The further processing of these effects are left for future studies.

Acknowledgements

This work is financially supported by the National Natural Science Foundation of China [No. 51901132]. We are also grateful to the financing of TESCAN CHINA, Ltd.

Data Availability

The 40×30 EBSPs of resolution 1140×1600 pixels are available at Zenodo (DOI: 10.5281/zenodo.5803072), together with the indexed crystal orientations and calibrated PC coordinates with a single BSE energy and the calibrated BSE energy fields. We invite interested colleagues to use this dataset to further improve the accuracy of EBSD indexation.

References

[1] S.I. Wright and B.L. Adams. Automatic analysis of electron backscatter diffraction patterns. *Metallurgical Transactions A*, 23(3):759–767, 1992.

[2] D. Jha, S. Singh, R. Al-Bahrani, W. Liao, A. Choudhary, M. De Graef, and A. Agrawal. Extracting grain orientations from EBSD patterns of polycrystalline materials using convolutional neural networks. *Microscopy and Microanalysis*, 24(5):497–502, 2018.

[3] A.J. Wilkinson, G. Meaden, and D.J. Dingley. High-resolution elastic strain measurement from electron backscatter diffraction patterns: New levels of sensitivity. *Ultramicroscopy*, 106(4-5):307 – 313, 2006.

[4] A. J. Wilkinson and T. B. Britton. Strains, planes, and EBSD in materials science. *Materials Today*, 15:366–376, 2012.

[5] E. Plancher. *Full-field measurements of elastic and total strains for the determination of the local behaviour in polycrystals*. PhD thesis, Ecole nationale supérieure d'arts et métiers - ENSAM, December 2015.

[6] T. Vermeij and J.P.M. Hoefnagels. A consistent full-field integrated DIC framework for HR-EBSD. *Ultramicroscopy*, 191:44 – 50, 2018.

[7] T.J. Ruggles, G.F. Bomarito, R.L. Qiu, and J.D. Hochhalter. New levels of high angular resolution EBSD performance via inverse compositional Gauss-Newton based digital image correlation. *Ultramicroscopy*, 195:85 – 92, 2018.

[8] Q. Shi, S. Roux, F. Latourte, and F. Hild. Estimation of elastic strain by integrated image correlation on electron diffraction patterns. *Ultramicroscopy*, 199:16–33, 2019.

[9] C. Ernould, B. Beausir, J.-J. Fundenberger, V. Taupin, and E. Bouzy. Global DIC approach guided by a cross-correlation based initial guess for HR-EBSD and on-axis HR-TKD. *Acta Materialia*, 191:131 – 148, 2020.

[10] T. Vermeij, M. De Graef, and J. Hoefnagels. Demonstrating the potential of accurate absolute cross-grain stress and orientation correlation using electron backscatter diffraction. *Scripta Materialia*, 162:266 – 271, 2019.

[11] C. Maurice, R. Fortunier, J. Driver, A. Day, K. Mingard, and G. Meaden. Comments on the paper "Bragg's law diffraction simulations for electron backscatter diffraction analysis" by Josh Kacher, Colin Landon, Brent L. Adams and David Fullwood. 110(7):758 – 759.

[12] B.E. Jackson, J.J. Christensen, S. Singh, M. De Graef, D.T. Fullwood, E.R. Homer, and R.H. Wagoner. Performance of dynamically simulated reference patterns for cross-correlation electron backscatter diffraction. *Microscopy and Microanalysis*, 22(4):789–802, 2016.

[13] S. Vespucci, G. Naresh-Kumar, C. Trager-Cowan, K. P. Mingard, D. Maneuski, V. O'Shea, and A. Winkelmann. Diffractive triangulation of radiative point sources. *Applied Physics Letters*, 110(12):124103, 2017.

[14] G. Nolze, M. JÜrgens, J. Olbricht, and A. Winkelmann. Improving the precision of orientation measurements from technical materials via EBSD pattern matching. *Acta Materialia*, 159:408 – 415, 2018.

[15] E.L. Pang, P.M. Larsen, and C.A. Schuh. Global optimization for accurate determination of EBSD pattern centers. *Ultramicroscopy*, 209:112876, 2020.

[16] A. Foden, D.M. Collins, A.J. Wilkinson, and T.B. Britton. Indexing electron backscatter diffraction patterns with a refined template matching approach. *Ultramicroscopy*, 207:112845, 2019.

[17] T. Tanaka and A.J. Wilkinson. Pattern matching analysis of electron backscatter diffraction patterns for pattern centre, crystal orientation and absolute elastic strain determination - accuracy and precision assessment. *Ultramicroscopy*, 202:87–99, 2019.

[18] Q. Shi, D. Loisnard, C. Dan, F. Zhang, H. Zhong, H. Li, Y. Li, Z. Chen, H. Wang, and S. Roux. Calibration of crystal orientation and pattern center of EBSD using integrated digital image correlation. *Materials Characterization*, 178:111206, 2021.

[19] T. Friedrich, A. Bochmann, J. Dinger, and S. Teichert. Application of the pattern matching approach for EBSD calibration and orientation mapping, utilising dynamical EBSP simulations. *Ultramicroscopy*, 184:44 – 51, 2018.

[20] Q. Shi, Y. Zhou, H. Zhong, D. Loisnard, C. Dan, F. Zhang, Z. Chen, H. Wang, and S. Roux. Indexation of electron diffraction patterns at grain boundaries. *Materials Characterization*, 182:111553, 2021.

[21] A. Winkelmann, B. Jablon, V. Tong, C. Trager-Cowan, and K. Mingard. Improving EBSD precision by orientation refinement with full pattern matching. *Journal of Microscopy*, 277(2):79–92, 2020.

[22] A. Winkelmann and G. Nolze. Analysis of kikuchi band contrast reversal in electron backscatter diffraction patterns of silicon. *Ultramicroscopy*, 110:190–194, 2010.

[23] F. Ram and M. Graef. Energy dependence of the spatial distribution of inelastically scattered electrons in backscatter electron diffraction. *Physical review. B, Condensed matter*, 97:134104, 2018.

[24] A. Winkelmann, T.B. Britton, and G. Nolze. Constraints on the effective electron energy spectrum in backscatter Kikuchi diffraction. 99:064115, 2019.

[25] A. Winkelmann. Dynamical effects of anisotropic inelastic scattering in electron backscatter diffraction. *Ultramicroscopy*, 108(12):1546–1550, 2008.

[26] A. Winkelmann, G. Nolze, G. Cios, T. Tokarski, P. Bala, B. Hourahine, and C. Trager-Cowan. Kikuchi pattern simulations of backscattered and transmitted electrons. *Journal of Microscopy*, 284(2):157–184, 2021.

[27] A. Winkelmann, C. Trager-Cowan, F. Sweeney, A.P. Day, and P. Parbrook. Many-beam dynamical simulation of electron backscatter diffraction patterns. *Ultramicroscopy*, 107(4):414 – 421, 2007.

[28] A. Wang and M. De Graef. Modeling dynamical electron scattering with bethe potentials and the scattering matrix. *Ultramicroscopy*, 160:35 – 43, 2016.

[29] C. Zhu and M. De Graef. EBSD pattern simulations for an interaction volume containing lattice defects. *Ultramicroscopy*, 218:113088, 2020.

[30] F. Ram, S. Zaefferer, T. Jäpel, and D. Raabe. Error analysis of the crystal orientations and disorientations obtained by the classical electron backscatter diffraction technique. *Journal of Applied Crystallography*, 48(3):797–813, 2015.

[31] F. Ram, S. Wright, S. Singh, and M. De Graef. Error analysis of the crystal orientations obtained by the dictionary approach to EBSD indexing. *Ultramicroscopy*, 181(Supplement C):17 – 26, 2017.

[32] B. Gaskey, L. Hendl, X. Wang, and M. Seita. Optical characterization of grain orientation in crystalline materials. *Acta Materialia*, 194:558 – 564, 2020.

[33] S.I. Wright, M. Nowell, S.P. Lindeman, P. Camus, M. De Graef, and M.A. Jackson. Introduction and comparison of new EBSD post-processing methodologies. *Ultramicroscopy*, 159, Part 1:81 – 94, 2015.

[34] M. Jackson, E. Pascal, and M. Graef. Dictionary indexing of electron back-scatter diffraction patterns: a hands-on tutorial. *Integrating Materials and Manufacturing Innovation*, 8:226–246, 2019.

[35] C. Zhu, C. Kurniawan, M. Ochsendorf, D. An, S. Zaefferer, and M. De Graef. Orientation, pattern center refinement and deformation state extraction through global optimization algorithms. *Ultramicroscopy*, 233:113407, 2022.

[36] J. Alkorta. Limits of simulation based high resolution EBSD. *Ultramicroscopy*, 131:33 – 38, 2013.

[37] D. Drouin, A.R. Couture, D. Joly, X. Tastet, V. Aimez, and R. Gauvin. CASINO v2. 42–a fast and easy-to-use modeling tool for scanning electron microscopy and microanalysis users. *Scanning*, 29(3):92–101, 2007.

[38] F. Hild and S. Roux. Digital image correlation. In P. Rastogi and E. Hack, editors, *Optical Methods for Solid Mechanics. A Full-Field Approach*, pages 183–228. Wiley-VCH, Weinheim (Germany), 2012.

[39] H. Zhong, Q. Shi, Z. Chen, C. Dan, S. Zhong, and H. Wang. Residual-based pattern center calibration in high-resolution electron backscatter diffraction. *Micron*, 146:103081, 2021.

[40] T.B. Britton, C. Maurice, R. Fortunier, J.H. Driver, A.P. Day, G. Meaden, D.J. Dingley, K. Mingard, and A.J. Wilkinson. Factors affecting the accuracy of high resolution electron backscatter diffraction when using simulated patterns. *Ultramicroscopy*, 110(12):1443 – 1453, 2010.

[41] D. Fullwood, M. Vaudin, C. Daniels, T. Ruggles, and S.I. Wright. Validation of kinematically simulated pattern HR-EBSD for measuring absolute strains and lattice tetragonality. *Materials Characterization*, 107(Supplement C):270 – 277, 2015.

[42] A. Winkelmann. *Dynamical Simulation of Electron Backscatter Diffraction Patterns*, pages 21–33. Springer US, 2009.

[43] K. Mingard, A. Day, C. Maurice, and P. Quested. Towards high accuracy calibration of electron backscatter diffraction systems. *Ultramicroscopy*, 111(5):320 – 329, 2011.

[44] J. Alkorta, M. Marteleur, and P.J. Jacques. Improved simulation based HR-EBSD procedure using image gradient based DIC techniques. *Ultramicroscopy*, 182:17 – 27, 2017.

[45] G. Nolze, T. Tokarski, G. Cios, and A. Winkelmann. Manual measurement of angles in backscattered and transmission Kikuchi diffraction patterns. *Journal of Applied Crystallography*, 53(2):435–443, 2020.

[46] E. Plancher, J. Petit, C. Maurice, V. Favier, L. Saintoyant, D. Loisnard, N. Rupin, J.-B. Marijon, O. Ulrich, M. Bornert, J.-S. Micha, O. Robach, and O. Castelnau. On the accuracy of elastic strain field measurements by Laue microdiffraction and high-resolution EBSD: a cross-validation experiment. *Experimental Mechanics*, 56(3):483–492, 2016.